Concept for a 3D-printed soft rotary actuator driven by a shape-memory alloy

Han Yuan, Frédéric Chapelle, Jean-Christophe Fauroux, Xavier Balandraud

Concept for a 3D-printed soft rotary actuator driven by a shape-memory alloy

Han Yuan[1,2], Frédéric Chapelle[2], Jean-Christophe Fauroux[2], and Xavier Balandraud[2,*]

[1] School of Mechanical Engineering and Automation, Shenzhen Graduate School, Harbin Institute of Technology, University Town of Shenzhen, 518055 Shenzhen, P.R. China

[2] Université Clermont Auvergne, CNRS, SIGMA Clermont, Institut Pascal, F-63000 Clermont-Ferrand, France

Abstract

In line with the recent development of soft actuators involving shape-memory alloys (SMAs) embedded in compliant structures, this paper proposes a concept for a rotary actuator driven by a SMA wire placed inside a 3D-printed helical structure. The concept consists of using the one-way memory effect of the SMA (activated by Joule heating) to create the rotation of a material point of the structure, while the inverse rotation is obtained during the return to ambient temperature thanks to the structure's elasticity. The study was performed in three steps. First, a prototype was designed from a chain of design rules, and tested to validate the feasibility of the concept. Thermal and geometrical measurements were performed using infrared and visible-range stereo cameras. A clockwise rotation (250°) followed by an anti-clockwise rotation (-200°) were obtained, enabling us to validate the concept despite the partial reversibility of the movement. Second, finite element simulations were performed to improve rotation reversibility. The high compliance of the mechanical system required a framework of large displacements for the calculations (in the strength of materials sense), due to the high structural flexibility. Finally, a second prototype was constructed and tested. Attention was paid to the rotation (fully reversible rotation of 150° reached) as well as to parasitic movements due to overall structural deformation. This study opens new prospects for the design and analysis of 3D-printed soft actuators activated by smart materials.

Keywords: soft rotary actuator, shape-memory alloy, design methodology, 3D-printing, experimental validation, infrared thermography

1. Introduction

Soft actuators are currently generating strong interest in research for various applications, while shape-memory alloys (SMAs) are more and more frequently being used as actuation systems attached to deformable structures: see for instance Refs. [1–9]. SMAs are active and smart materials whose mechanical properties are triggered by temperature and stress. They exhibit several thermomechanical properties which are spectacular for metallic materials [10–12]: superelasticity or pseudoelasticity, one-way memory effect, several types of two-way memory effect, rubber-like effect, as well as strong damping capacities depending on their operating temperature. Macroscopically, superelasticity is characterized by a reversible stretching of several per-cent after a load-unload cycle at constant ambient temperature. The memory effect corresponds to the ability to return to a given shape by heating of the SMA component. The occurrence of the effects depends on the work temperatures (see Section 2.1 for a reminder about SMAs). SMAs have found numerous applications in robotics [13–15]. In addition, they can be used in morphing aircraft technology [16], the design of miniature mechanical devices [17], and medical rehabilitation and neuroscience [18]. In the context of the present study, we highlight SMA-based actuators, for which two review papers have recently been published: Ref. [19] for linear actuators and Ref. [20] for rotary actuators. These references show the need to design original architectures having a high level of component integration to ensure the transformation of the shape memory effect into a desired motion. The architectures rely on a given form of SMA components and specific attachment points within the actuator structure [21–27]. Some specific aspects of the research on soft actuating devices using SMAs have been discussed in the literature: compactness and light weight [28–34], impact of flexible parts on mechanical outputs [35, 36], twisting type of movement [27–39], impact of curved shapes on actuator performance [40], thermal response of the SMA component [41].

The present study deals with the design and evaluation of an innovative rotary actuator driven by a SMA wire placed on a 3D-printed monolithic soft structure featuring a helical shape. The proposed concept is as follows: the one-way memory effect of the SMA is used to create a rotation of a material point of the structure, while the inverse rotation is obtained thanks to the elasticity of the structure during the return to ambient temperature of the SMA wire. Using our classification proposed in Ref. [20], this actuator concept belongs thus to the following sub-classification: *actuators with non-continuous rotation* > *with bi-directional rotation* > *driven by one SMA element and one bias spring*. The "bias spring" here is the monolithic soft structure.

The study was performed in three steps. First, a prototype was designed using a methodology based on the chaining of design rules. It was then constructed and tested for concept validation purposes (see Section 2). Experiments consisted of thermal and geometrical measurements using infrared and visible-range stereo cameras, respectively, in order to follow the progression of the system during the tests. In the second step, finite element simulations were performed to improve the prototype in terms of the reversibility of the obtained rotation (see Section 3). In the final step, a new demonstrator was constructed and tested, with a focus on rotation as well as on parasitic movements due to overall structure deformation (see Section 4).

2. Development and experimental validation of the concept

This section presents the first prototype to be designed, constructed and tested. First, a brief reminder about SMAs is presented to provide the necessary information for the next sections.

2.1. SMA background

Let us first recall the properties of SMAs with a focus on the so-called one-way memory effect, which is the property used in the present study. The reader is referred to Refs. [10–12] for more details about the different thermomechanical and metallurgical properties of these active materials. The specific performances of SMAs originate in a solid-to-solid reversible phase transition. With reference to steels, the two crystallographic phases are named *austenite* and *martensite*. A SMA sample can be either purely austenitic (A), purely martensitic (M) or a mixture of the two phases (A+M), depending on temperature and stress: see Figure 1. Austenite and martensite are obtained at "high" and "low" temperatures respectively. At zero stress, the M→A transformation starts at temperature A_s (austenite-start) and finishes at temperature A_f (austenite-finish), while the reverse transformation A→M starts at temperature M_s (martensite-start) and finishes at temperature M_f (martensite finish). These four transformation temperatures depend on the chemical composition and on the elaboration process, which involves cold working and heat treatment. During a heating-cooling cycle, a transformation hysteresis is usually observed: $M_f < A_s$ and $M_s < A_f$.

Insert here Figure 1: Simplified state diagram of a SMA and steps for the one-way memory effect.

It is important to note that the martensite phase features different "variants", which correspond to the same crystal structure but with different orientations in space with respect to the austenite crystal, each one being associated with a specific *transformation strain*. The proportions of the *martensite variants* depend on the macroscopic stretch imposed on the SMA sample. As a consequence, different shapes can be obtained for a martensitic sample. A shape can be "frozen" by stretching, corresponding to a change in the proportions of martensite variants. On the contrary, the austenitic state is characterized by a unique shape. Elastic strains obviously also exist as a function of the loading, in addition to the transformation strains.

When an austenite sample is cooled down below M_f (A→M transformation) at zero stress, martensite variants appear in equal proportions, leading to no macroscopic shape change in the SMA sample. Such a martensite, featuring equal proportions of variants, is referred to as

auto-accommodating martensite. On the contrary, martensite with different proportions of variants is referred to as *oriented martensite*. A SMA sample comprising oriented martensite is thus in a deformed state with respect to the reference shape (austenitic state, or self-accommodating martensitic state). The one-way memory effect corresponds to a transformation from oriented martensite to austenite by heating. For nickel-titanium-based (Ni-Ti-based) SMAs, recoverable axial strains of several per-cent are possible, typically 5-6%. The one-way memory effect is generic for SMAs. A two-way memory effect at zero stress is possible after material training, but the process requires a specific metallurgical optimization to achieve sufficient stability [42]. SMA components devoted to actuation are usually martensitic at ambient temperature ($T_{amb} < M_f$), see Figure 1. This configuration enables the shape setting of the SMA at ambient temperature, while the activation of the memory effect is simply performed by heating above ambient. Based on this reminder about SMAs, the next section presents the design methodology that was applied to propose a prototype rotary actuator.

2.2. Design rules

The design approach, first presented in Ref. [43], is based on the chaining of design rules: see Figure 2. Requirement Constraints (RC) are expressed, and then reformulated separately into Design Rules (DR). The latter are constraints that can be combined and transformed progressively by inference or restriction (when one choice is made among many others) into a new set of constraints. The last operation is embodiment, which proposes a concrete Design Feature (DF) as a solution to a constraint set. By regrouping all the DFs, a final embodiment can be proposed. This methodology enables the design space to be explored, even partially, keeping trace of the current design process. It allows subsequent modifications and, when no solution can be found, emphasizes where to search in the design space. The specifications here concern the design of a SMA-driven rotary actuator with a hollow shaft for bi-directional motion with a limited angular stroke. They are inherited from a previous robotic project [44], with potential applications on several scales. This section examines the RCs and the derived DRs and DFs.

Insert here Figure 2: Design method based on the chaining of design rules.

• RC1: bi-directional rotation is sought. Three Design Rules can be considered to satisfy this requirement:

- DR1a: using a SMA component with a two-way memory effect;
- DR1b: using two SMA components with a one-way memory effect, acting in opposition;
- DR1c: using a single SMA component with a one-way memory effect, in opposition with a compliant structure acting as a bias spring.

DR1a was considered as not being relevant because SMAs with a two-way memory effect have lower performances in terms of stability and recoverable deformation amplitude. They are also much more expensive. DR1b and DR1c have already been used in many rotary actuators described in the literature [20]. In particular, DR1c has been employed in mechanisms using steel bias springs. However, DR1c has not been used so much with a compliant structure whose geometry is optimized to create a rotary actuator. So DR1c was selected to design an innovative rotary actuator.

• RC2: small or null sliding between the SMA component and the compliant structure is sought in order to minimize efficiency loss. This requirement derives from previous research works which have shown that there is very high friction for a SMA wire coiled on a supporting cylinder [20, 45]. In agreement with Ref. [5], a possible design rule is "DR2: the actuator will use the principle of differential bending". This principle is commonly implemented with bimetallic strips in thermal switches. Gluing together two strips of different metals avoids any relative sliding between them, and the difference in strains between the strips is transformed into strip bending.

• RC3: a compact hollow-shafted actuator is sought. This is simply interpreted by Design Rule "DR3: a tubular shape is chosen for the system".

By combining DR1-3, the bi-layer linear beam of DR2 has to be circularly curved. This leads to a first Design Feature DF1: a bi-layer circular beam (a layer of SMA component and a

second layer of material acting here as a bias spring, see DR1c), curved along a certain winding angle to be determined below.

• RC4: the rotation stroke of the actuator should reach a given value θ_{max}. Let us consider a recoverable axial strain ε_{SMA} of the SMA component at the martensitic static (several per-cent for Ni-Ti-based SMAs). The thermal activation of the one-way memory effect leads the SMA component to return to its initial length. The resulting design rule emerges, based on a circular beam (DR3) featuring several turns: "DR4: the number of turns N_t of the circular beam depends on the required angular stroke θ_{max} and on the recoverable strain ε_{SMA} of the SMA through Equation 1".

$$N_t = \frac{\theta_{max}}{2\pi \times \varepsilon_{SMA}} \quad (1)$$

Note that the beam curvature radius is expected to change during rotation due to overall structure deformation, justifying a modification to Equation 1:

$$N_t = \frac{\theta_{max}}{2\pi \times \left[1-\frac{R}{R'} \times (1-\varepsilon_{SMA})\right]} \quad (2)$$

where R and R' are the initial and current curvature radii of the beam respectively. R' can be estimated by finite element simulation, for instance (see Section 3).

Several Design Features can then be proposed for the geometry of the beam and the SMA component, as well as for the connection between them:

- DF2: multi-turn embodiment can now be defined. Inferring the possible geometric aspect of the system leads to two possible alternatives for the Design Feature describing the general shape of the actuator: DF2a: plane spiral; or DF2b: helix. The DF2b configuration was chosen here because it maintains a constant curvature radius R compatible with Equations 1 or 2. Consequently, our demonstrator will be based on a helix, all along which a SMA component is fixed. DF2a could be explored for other

applications, provided a suitable calculation for the number of turns with variable curvature can be found;

- DF3: elementary SMA components are mainly sold in the form of wires, springs, foils, sheets, bars and tubes. We propose to use a wire because it is the most common form available. Moreover, this form is easy to curve in a helical shape, as required by DF2b. For the beam, a rectangular cross-section was chosen;
- DF4: two fixture solutions are proposed to comply with Design Rule DR6 "The SMA wire should remain in permanent contact with the supporting beam". These are DF4a: SMA wire inserted into a helical hole made in the supporting beam, and DF4b: SMA wire sandwiched between two helices of thickness h_1 and h_2. The latter solution was selected because DF4a was expected to lead to difficult manufacturing and insertion operations;
- DF5: Figure 3 shows the geometric parameters considered for the helical structure. Several Design Rules are involved here:
    - DR5: the interval $b+i$ between the turns should be as small as possible to take better advantage of the change in length of the SMA wire (maximizing the rotation);
    - DR7: the helical beam cross-section $b \times h$ should be large enough to resist the compression applied by the SMA wire when it returns to its original shape (risk of buckling);
    - DR8: the height h of the helical beam section enables the bending quadratic moment I_{zz} of the support to be adjusted, assuming that the two helices of thickness h_1 and h_2 are carefully bonded;
    - DR9: h_1/h_2 should be as large as possible in order to maximize differential bending.

Insert here Figure 3: Geometric parameters for the helical structure.

Finally, additional rules were elaborated concerning the materials of the system:

- DR10: the SMA wire must be stretched in the martensitic state (at ambient temperature) to ensure the correct memory effect afterwards. Concerning the transformation temperatures of the SMA wire, the following Design Feature must therefore be used. DF7: M_f and A_f must be higher than ambient temperature T_{amb} (*e.g.* 20°C) and lower than the maximum temperature T_{max} of the heated SMA wire;
- DR11: the thermal activation of the memory effect should be simple, typically by Joule heating;
- DR12: the helix support should resist the heating of the SMA wire. T_{max} should be limited to some tens of Celsius degrees, *e.g.* 100°C maximum;
- DR13: the helix support should guarantee the electrical insulation of the SMA wire.

The material choice derives from several design rules: DR12 imposes that the helix material must withstand the heating of the SMA wire; DR13 imposes a dielectric material. DRs 7-9 and 11-13 oriented us towards fast prototyping by polymer 3D-printing to elaborate the helix. In addition, this type of manufacturing method is interesting for the optimization of the prototype in future works. Based on these general choices, the next section provides the details of the first prototype which was constructed.

2.3. First prototype

Figure 4 presents the prototype designed to validating the concept of a rotary actuator driven by a SMA wire placed on a monolithic soft structure. A Ni-Ti-based SMA wire, 1 mm in diameter, provided by Nimesis (France) was chosen. It featured the following transformation temperatures: M_f = 24°C, M_s = 48°C, A_s = 57°C and A_f = 73°C. It is thus martensitic at ambient temperature, in agreement with DF7 in Figure 2. Its maximum recoverable strain was of 5%. Its onset of martensite orientation was of 20 MPa. Before being placed in the supporting helix, the SMA wire must be prepared:

- step (1): heating above A_f using a hot-air dryer and return to ambient temperature at zero stress in order to create self-accommodating martensite;
- step (2): stretching in tension using an external device to create oriented martensite.

The obtained strain corresponds to the parameter ε_{SMA} which was introduced in Equations 1 and 2 above;

- step (3): wrapping the SMA wire onto the inner part of the helix, and placement of the external part.

Insert here Figure 4: First prototype of SMA-driven rotary actuator: a) cross-section of the system, b) photo of the system. A 3D-printed ABS helix was used as a supporting structure, and a Ni-Ti-based SMA wire was placed in a groove between the two parts of the helix.

Two solutions were envisaged concerning the material of the supporting helix. Polylactic acid (PLA) was first tested, see DF8a. A collapse of the helix was observed at around 60-80°C during the thermal activation of the SMA wire. Successful tests were then performed using acrylonitrile butadiene styrene (ABS), see DF8b. Indeed, the glass transition temperature T_g of ABS is 105°C, which is above the A_s temperature of the SMA, in agreement with DF7 in Figure 2. The two parts of the helix were printed separately, as per DF4b. Both were plain, *i.e.* without an internal void. The values of the geometric parameters are given in Figure 4-a. The thermal distortions due to 3D-printing process were limited with the chosen geometric parameters. An anchorage system was used at each end of the helix to fix the SMA wire (see DF6 and Fig. 4-b). It was simply constructed of two pairs of small metallic plates tightened by screws.

2.4. Experimental set-up

Figure 5 presents the experimental set-up used for the tests. The helical structure containing the SMA wire was placed vertically and fixed at its bottom end. The set-up also comprised a power generator, a voltmeter and an ammeter. Two means of measurement were employed:

- two visible-range stereo cameras were used to measure the movement of the free end of the helix: a Xtion Pro Live camera (ASUS) was placed above the mechanical system,

while a Bumblebee2 1394a (FLIR) camera was placed perpendicularly to the helix axis (see Fig. 5-a);

- tests were performed using a Cedip Jade III-MWIR infrared camera to measure the temperature of the system. For these tests, the prototype was placed in a cardboard box to limit parasitic reflections in the infrared range (see Fig. 5-b). Moreover, the external part of the helix was not present (only the inner part was used), leaving the SMA wire visible. It was thus possible to measure the temperature of both the SMA wire and the helix with the infrared camera. Note that for these measurements, the observed surfaces were painted in black prior to testing in order to maximize their thermal emissivity (0.96).

Insert here Figure 5: Experimental set-up: a) use of 3D vision cameras to measure the movement of the free end of the helix, b) use of an infrared camera to measure temperature variations during the thermal activation of the SMA wire.

2.5. Results, analysis and conclusion for the first prototype

The following test conditions were applied for the purpose of concept validation:

- steps (1) to (3): see section 2.3 above. The strain ε_{SMA} was set to 1.4%, for a rotation expected to be greater than 200° from Equation 2;
- step (4): heating of the SMA wire by Joule effect with a constant current intensity of 3.5 A, up to rotation stabilization;
- step (5): natural return to ambient temperature by switching off the electric current.

Ambient temperature T_{amb} was equal to 20°C. Figure 6 presents the results of the thermal analysis. The surface temperatures in steady-state regime are shown in Figure 6-a. Let us recall that only the inner layer of the helix was retained for the thermal measurements (see Section 2.4): point A is located on the SMA wire, while point B is on internal radial surface of the helix. It can be seen that the temperature pattern is quite homogeneous along the helix,

except at the helix extremity due to the anchorage system. Figure 6-b shows the steady temperatures at points A and B for different values of current intensity. In practice, a waiting time of 10 minutes was applied at constant intensity before capturing the thermal image. The temperature of the SMA wire approached 90°C for an intensity of 3.5 A, which was enough to fully activate the memory effect (A_f = 73°C) without stiffness loss and degradation of the ABS plastic (T_g = 105°C). By thermal conduction, the temperature of the helix also increased (see values at point B). As expected, the helix acts as a thermal insulator of the SMA wire, which in practice prevents a rapid return to ambient temperature.

Insert here Figure 6: Thermal analysis of the first prototype: a) surface temperature in steady-state regime for an electric current intensity of 3.5 A, b) steady temperature at points A and B for different current intensities. Point A is located on the external radial surface. Point B is located on the internal radial surface of the helix.

The bottom end of the helix being fixed, the objective here is to analyze the rotation θ of the top end (around the helix axis) during the thermal cycle of the SMA wire. Figure 7 presents the variation in θ during the test. A clockwise rotation (250°) followed by an anti-clockwise rotation was obtained, enabling us to validate the concept of actuation. However, a residual angle of about 50° was observed at the end of the thermal cycle (see Fig. 7-d). After carefully removing the SMA wire from the helical structure, a residual deformation of the latter was observed: a plastic process had occurred in the helix. It was then proposed to improve the actuator in terms of movement reversibility from numerical simulations, as presented in the next section.

Insert here Figure 7: Variation in rotation angle θ during a thermal cycle on the first prototype. Bidirectional rotation was successfully obtained, but a residual angle remained at the end of the test (time t_2).

3. Improvement of the actuator from simulation results

In order to ensure the reversibility of the rotational movement of our actuator, some parameters had to be modified compared to the first prototype. The objective was to avoid a plastic response in the helix. Numerical simulations were used for this purpose.

3.1. Problem

From design rules DRs 10-13, we chose to keep the same SMA wire and the same 3D-printed material. Based on the promising results obtained with the first prototype, we proposed also to keep the principle of a helix shape for the 3D-printed structure, as well as the same length for the SMA wire. In practice, the following parameters were kept constant: $N_s = 5$, $R = 44$ mm, $b + i = 22$ mm (see Fig. 4). Finally, as the tests performed with the infrared camera were successful without the external part of helix (only the inner part was retained), it was decided to simply remove this external part: $h_2 = 0$ and $h_1 = h = 4$ mm. This configuration is also relevant with respect to design rule DR9. The objective was thus to propose new values for the following parameters:

- the recoverable axial strain ε_{SMA} of the SMA wire,
- the dimensions of the helix beam cross section, h and b,

such that the maximum Von Mises stress in the helix remains below the yield stress of the material. Table 1 provides the known values for the problem. The mechanical properties of our ABS material was first identified from a tensile test, as described in the following section.

Insert here Table 1: Parameters chosen for finite element simulations.

3.2. Mechanical characterization of the ABS 3D-printed polymer

Whereas the properties of the SMA wire were known from the supplier datasheet, those of the ABS material needed to be identified, as they were expected to vary depending on the

elaboration process parameters. Figure 8 shows the strain-stress curve in tension of the 3D-printed ABS material featuring a filling rate of 100%. Young's modulus, conventional elastic limit at 0.2% and strength were identified as E_{ABS} = 1.55 GPa, $Re_{0.2}$ = 14.7 MPa and Rm = 18.6 MPa, respectively. In fact, the mechanical response started to become non-linear from about 5 MPa. This value was considered as the material yield stress that must not be exceeded to guarantee the mechanical reversibility of the actuator movement: Re = 5 MPa. It can be finally noted that, even though the stiffness in tension of the material may seem high (order of magnitude of one gigapascal), the highly flexible character of our actuator is due to its helical geometry.

Insert here Figure 8: Strain-stress curve in tension of the 3D-printed ABS material.

3.3. Numerical modeling and results

Finite element simulations were performed using the Ansys package. Quadratic hexahedron elements (Solid186) were used, as well as quadratic quadrilateral elements (Conta174 and Target170) for the contact between the SMA wire and the helix. Only one turn of the helix was considered, in order to reduce calculation times: see Figure 9-a. The numbers of nodes and elements were equal to 689,140 and 149,364 respectively. As the number N_t of turns for the whole helix was equal to 5, kinematic output data must be then multiplied by 5. It gives for the rotation angle along the helix axis: $\theta = 5 \times \theta_{one\text{-}turn}$, where $\theta_{one\text{-}turn}$ is the rotation deduced from the simulation. The thermal analysis in Figure 6 showed that the temperature in the main part of the ABS helix reached 55°C (for the maximum heating of the SMA wire, at 3.5 A), while the contact temperature with the SMA wire approached 90°C. As the glass transition temperature T_g of ABS plastic is of 105°C, the influence of temperature was neglected in the simulations in terms of stiffness variation.

Insert here Figure 9: Finite element analysis performed: a) geometry and mesh of one turn of the helix with SMA wire, b) Von Mises stress field using the parameters in Tables 1 and 2, c) top view before and after the thermal activation of the SMA wire.

Boundary conditions consisted of setting to zero all the degrees of freedom at one extremity of the system (end sections of both helix and SMA wire). At the other extremity, nodes between the helix and the SMA wire were merged to model the anchorage of the two components. Calculations were performed within the framework of large displacements (in the strength of materials sense), meaning that mechanical equilibrium shall be verified on the deformed geometry (and not on the reference undeformed configuration). Even if it leads to much longer calculation times (non-linear model), this solving framework was necessary in order to precisely obtain the deformed state of the mechanical system [46]. Indeed, the softness of the rotary actuator is due to a high "structural" compliance (and not a "material" compliance), justifying a simulation framework of small strains and large displacements.

Isotropic linear elastic "small-strain" behavior was considered for the helix. The behavior of the SMA wire was modeled using a simple approach [47]: the initial state at zero stress is considered as the (deformed) oriented martensite state, and the return to austenite is obtained by shifting the zero-stress state by -ε_{SMA}. The orientation process of the martensite at ambient temperature was not modeled. The input data of our simulation to obtain the final state of the system are the elastic properties of the materials (Young's modulus and Poisson's ratio) at high temperature and the quantity ε_{SMA}. Even if this approach is basic, it provides a first-order value of the final displacement of the mobile end of the helix without the requirement of complex models for the SMA material. The approach provides the final state of the system (when the SMA wire is returned to austenite state) but not the kinetics of phase transformation as a function of the temperature.

Simulations showed that very high Von Mises stresses are located at the free end of the helix (Fig. 9-b). This is due to the boundary conditions at the merging of the nodes common to the two materials, creating a geometric singularity. For this reason, the maximum Von Mises

stress value σ_{max} which was considered for the analysis was extracted 5 mm from the free end. As expected, decreasing more and more the parameter h (for fixed values of b and ε_{SMA}) tends to increase σ_{max}; the same is true for the influence of parameter b for fixed values of h and ε_{SMA}. Thus it was decided to keep the overall dimensions of the beam as in the first prototype (b = 12 mm and h = 4 mm) and to optimize only the recoverable strain ε_{SMA} of the SMA wire. Figure 10 shows the variations in σ_{max} and $\theta_{one\text{-}turn}$ as a function of ε_{SMA}. The higher the value of ε_{SMA}, the higher the values of σ_{max} and $\theta_{one\text{-}turn}$. In order to prevent plasticity in the helix while maximizing the rotation angle, the configuration for which σ_{max} = 5 MPa (value of the yield stress *Re*) was considered as optimal: see path 1-2 in Figure 10-a. Table 2 shows the parameters obtained in this configuration: a rotation angle $\theta_{one\text{-}turn}$ of 30.3° is obtained for ε_{SMA} = 0.62% (see path 2-3 in Figure 10-b). For the whole helix with five turns, this gives θ = 5×30.3 = 151.5°. The next section provides an experimental verification using this configuration.

Insert here Figure 10: Identification of the recoverable strain ε_{SMA} of the SMA wire from simulations, with b = 12 mm, h = 4 mm and parameters given in Table 1: a) maximum Von Mises stress σ_{max} as a function of ε_{SMA}, b) rotation angle $\theta_{one\text{-}turn}$ as a function of ε_{SMA}.

Insert here Table 2: Results of the numerical simulations, guaranteeing the full reversibility of the rotation movement.

4. Experimental validation of the new rotary actuator prototype

A second prototype based on the above numerical analysis was constructed and tested. The reversibility of rotation is first verified. Final remarks are then provided about parasitic movements due to overall structure deformation.

4.1. Validation of the reversibility of the rotation movement

Figure 11 shows the variation in the rotation angle θ during a thermal cycle for the second prototype. An electric current intensity of 3.5 A was applied for the heating phase. The maximum rotation obtained was equal to 150°, which is very close to the simulated value. Clearly, the rotation movement was reversible: see the return to 0° at the end of the thermal cycle. It must be noted that the SMA wire worked in bending configuration, meaning that high levels of longitudinal stress can be reached with small curvatures. Moreover, small strains can lead to large displacements, in the strength of materials sense, because of the structural softness of the ABS helix. These two points explain why the relatively small stiffness of the ABS helix can produce the reverse rotation during the return to ambient temperature. An additional test was performed with the current intensity varying by steps of ±0.5 A up to 3.5 A: see Figure 12. Each stage lasted 400 s, which was the duration required for rotation stabilization. The reversibility of the movement was confirmed. It can be seen that intermediate rotations can be targeted between 0 and 150°. However, a strong non-linearity of the attained angle with respect with the applied electric intensity current can be noted. This response opens prospects for the control of the actuator in further studies.

Insert here Figure 11: Variation in the rotation angle θ during a thermal cycle for the second prototype using an electric current intensity of 3.5 A.

Insert here Figure 12: Variation in the rotation angle θ during a thermal cycle for the second prototype, with current intensities varying in steps of ±0.5 A.

4.2. Final remarks concerning overall structure deformation

In addition to the rotation of the free end of the helix, longitudinal and radial expansions were observed. These movements are due to the three-dimensional character of the structure deformation. The longitudinal expansion (along the helix axis) was measured using the second stereo camera, which was placed perpendicularly to the helix axis, while the top camera was used to follow the radial displacement of the helix free end. Figure 13 shows the variation in the

total length (along the helix axis), as well as the variation in the radius at the free end (perpendicularly to the helix axis), as a function of current intensity. Relative variations of 23% and 21% are visible for the radius and the length, respectively, for maximum heating. These parasitic movements are not negligible, and it will be necessary to reduce them for some practical applications, although this is out of the scope of the present study.

Insert here Figure 13: Variations in the total length (along the helix axis) and the radius at the free end of the helix (perpendicularly to the helix axis) as a function of current intensity.

5. Conclusion

An innovative concept for a SMA-driven rotary actuator was proposed and validated in this study. A SMA wire was placed on a 3D-printed monolithic soft structure acting as a bias spring: the one-way memory effect of the SMA was thermally activated by Joule heating to create the rotation of a material point of the structure, while the inverse rotation was obtained during the return to ambient temperature thanks to the structure's elasticity. From the chaining of design rules, and using finite element simulations, two demonstrators were designed, constructed and tested. Attention was paid to the reversibility of the rotation: a fully reversible rotation of about 150° was successfully obtained, validating our concept. The study provides an example of energy transduction in SMA, applied here to rotary actuation: from electrical energy to heat (by Joule effect), and finally to mechanical energy (due to the strong thermo-mechanical coupling in the SMA component). Two important prospects can be proposed:

- 3D-printing offers wide possibilities in terms of shapes for the monolithic structure, allowing us to imagine more complex movements for the actuator (not limited to single rotations), possibly involving several SMA wires;
- the proposed rotary actuator concept can easily accommodate size reduction. Homothetic reduction of the dimensions can be simply performed, within the limits of the performance of the 3D-printer and the availability of the SMA wires. For the

demonstrators constructed in the present study, only the anchorage system between the SMA wire and structure at the two ends of the helix should require modification (*e.g.* using glue instead of screws) to allow size reduction.

These two points open new routes for the design of soft actuators in applications requiring strong integration, typical of those already using compliant mechanisms (positioning, medical, etc.).

Acknowledgements

The authors would like to acknowledge the Region Auvergne for supporting this research within the MatGrid funding program.

References

[1] Wu R, Han M W, Lee G Y and Ahn S H 2013 Woven type smart soft composite beam with in-plane shape retention *Smart Mater. Struct.* **22** 125007

[2] Kim H J, Song S H and Ahn S H 2013 A turtle-like swimming robot using a smart soft composite (SSC) structure *Smart Mater. Struct.* **22** 014007

[3] Cianchetti M 2013 Fundamentals on the use of shape memory alloys in soft robotics. In: *Habib M K and Davim J P (eds) Interdisciplinary Mechatronics (Hoboken, NJ, USA: John Wiley & Sons)* chapter 10 pp 227–54

[4] Rodrigue H, Wei W, Bhandari B and Ahn S H 2015 Fabrication of wrist-like SMA-based actuator by double smart soft composite casting *Smart Mater. Struct.* **24** 125003

[5] She Y, Chen J, Shi H L and Su H J 2016 Modeling and validation of a novel bending actuator for soft robotics applications *Soft Robot.* **3** 71–81

[6] Jin H, Dong E B, Xu M, Liu C S, Alici G and Jie Y 2016 Soft and smart modular structures actuated by shape memory alloy (SMA) wires as tentacles of soft robots *Smart Mater. Struct.* **25** 085026

[7] Xiang C Q, Yang H, Sun Z Y, Xue B C, Hao L N, Rahoman M D A and Davis S 2017 The design, hysteresis modeling and control of a novel SMA-fishing-line actuator *Smart Mater. Struct.* **26** 037004

[8] Yang Y, Chen Y, Li Y, Chen M Z and Wei Y 2017 Bioinspired robotic fingers based on pneumatic actuator and 3D printing of smart material *Soft Robot.* **4** 147–62

[9] Rodrigue H, Wang W, Han M W, Kim T J Y and Ahn S H 2017 An overview of shape memory alloy-coupled actuators and robots *Soft Robot.* **4** 3–15

[10] Otsuka K and Wayman C M 1999 *Shape Memory Materials* (Cambride, UK: Cambridge University Press)

[11] Lagoudas D C 2010 *Shape Memory Alloys: Modeling and Engineering Applications* (New York, USA: Springer Science)

[12] Lexcellent C 2013 *Shape-Memory Alloys Handbook* (Hoboken, NJ, USA: John Wiley & Sons)

[13] Sreekumar M, Nagarajan T, Singaperumal M, Zoppi M and Molfino R 2007 Critical review of current trends in shape memory alloy actuators for intelligent robots *Ind. Robot. Int. J.* **34** 285–94

[14] Kheirikhah M M, Rabiee S and Edalat M E 2011 A review of shape memory alloy actuators in robotics. In: *Ruiz-del-Solar J, Chown E and Plöger P G (eds) RoboCup 2010: Robot Soccer World Cup XIV. Lecture Notes in Computer Science* (*Springer-Verlag Berlin Heidelberg)* vol 6556, pp 206-17

[15] Jani J M, Leary M, Subic A and Gibson M A 2014 A review of shape memory alloy research, applications and opportunities *Mater. Des.***56** 1078–113.

[16] Barbarino S, Flores E I S, Ajaj R M, Dayyani I and Friswell M I 2014 A review on shape memory alloys with applications to morphing aircraft *Smart Mater. Struct.* **23** 063001

[17] Nespoli A, Besseghini S, Pittaccio S, Villa E and Viscuso S 2010 The high potential of shape memory alloys in developing miniature mechanical devices: a review on shape memory alloy mini-actuators *Sensor Actuat. A-Phys.* **158** 149–60

[18] Pittaccio S and Viscuso S 2012 Shape memory actuators for medical rehabilitation and neuroscience. In: *Berselli G, Vertechy R and Vassura G (eds) Smart Actuation and Sensing Systems - Recent Advances and Future Challenges (Rijeka: Intech)* chapter 4 pp 83–120

[19] Mohd Jani J, Leary M and Subic A 2017 Designing shape memory alloy linear actuators: a review *J. Intell. Mater. Syst. Struct.* **28** 1699–718

[20] Yuan H, Fauroux J C, Chapelle F and Balandraud X 2017 A review of rotary actuators

based on shape memory alloys *J. Intell. Mater. Syst. Struct.* **28** 1863–85

[21] Zhang X and Yan X 2012 Continuous Rotatory Motor Actuated by Multiple Segments of Shape Memory Alloy Wires *J. Mater. Eng. Perform.* **21** 2643–9

[22] Manfredi L, Huan Y and Cuschieri A 2017 Low power consumption mini rotary actuator with SMA wires *Smart Mater. Struct.* **26** 115003

[23] Yan X, Huang D and Zhang X 2014 Note: A novel curvature-driven shape memory alloy torsional actuator *Rev. Sci. Instrum.* **85** 14–6

[24] Sheng J and Desai J P 2015 Design, modeling and characterization of a novel meso-scale SMA-actuated torsion actuator *Smart Mater. Struct.* **24** 105005

[25] Hwang D and Higuchi T 2014 A cycloidal wobble motor driven by shape memory alloy wires. *Smart Mater. Struct.* **23** 055023

[26] Lai C M, Chu C Y and Lan C C 2013 A two-degrees-of-freedom miniature manipulator actuated by antagonistic shape memory alloys *Smart Mater. Struct.* **22** 085006

[27] Paik J K, Hawkes E and Wood R J 2010 A novel low-profile shape memory alloy torsional actuator *Smart Mater. Struct.* **19** 125014

[28] Suzumori K, Endo S, Kanda T, Kato N and Suzuki H 2007 A bending pneumatic rubber actuator realizing soft-bodied manta swimming robot. In: *Robotics and Automation ICRA (Rome, Italy, April 10-14, 2007) IEEE International Conference on (New York, NY, USA: IEEE)* pp 4975–80

[29] Koo I M, Jung K, Koo J C, Nam J D, Lee Y K and Choi H R 2008 Development of soft-actuator-based wearable tactile display *IEEE Trans. Robot.* **24** 549–58

[30] Yang K and Gu C L 2008 A compact and flexible actuator based on shape memory alloy springs *Proc. Inst. Mech. Eng. Part C-J. Mech.* **222** 1329–37

[31] Tsagarakis N G, Laffranchi M, Vanderborght B and Caldwell D G 2009 A compact soft actuator unit for small scale human friendly robots. In: *Robotics and Automation ICRA (Kobe, Japan, May 12-17, 2009) IEEE International Conference on (New York, NY, USA: IEEE)* pp 4356–62

[32] Torres-Jara E, Gilpin K, Karges J, Wood R J and Rus D 2010 Compliant modular shape memory alloy actuators *IEEE Robot. Autom. Mag.* **17** 78–87

[33] Villoslada A, Flores A, Copaci D, Blanco D and Moreno L 2015 High-displacement

flexible shape memory alloy actuator for soft wearable robots *Robot. Auton. Syst.* **73** 91–101

[34] Leng J, Yan X, Zhang X, Huang D and Gao Z 2016 Design of a novel flexible shape memory alloy actuator with multilayer tubular structure for easy integration into a confined space *Smart Mater. Struct.* **25** 025007

[35] Guo Z, Pan Y P, We L B and Yu H Y 2015 Design and control of a novel compliant differential shape memory alloy actuator *Sensor Actuat. A-Phys.* **225** 71–80

[36] Mammano G S and Dragoni E. Modelling, simulation and characterization of a linear shape memory actuator with compliant bow-like architecture *J. Intell. Mater. Syst. Struct.* **26** 718–29

[37] Shim J E, Quan Y J, Wang W, Rodrigue H, Song S H and Ahn S H 2015 A smart soft actuator using a single shape memory alloy for twisting actuation *Smart Mater. Struct.* **24** 125033

[38] Song S H, Lee H, Lee J G, Lee J Y, Cho M and Ahn S H 2016 Design and analysis of a smart soft composite structure for various modes of actuation *Compos. Part B-Eng.* **95** 155–65

[39] Rodrigue H, Wang W, Han M W, Quan Y J and Ahn S H 2016 Comparison of mold designs for SMA-based twisting soft actuator *Sens. Actuators Phys.* **237** 96–106

[40] Rodrigue H, Wang W, Kim D R and Ahn S H 2017 Curved shape memory alloy-based soft actuators and application to soft gripper *Compos. Struct.* **176** 398–406

[41] Jin H, Dong E B, Alici G, Mao S X, Min X, Liu C S, Low K H and Yang J 2016 A starfish robot based on soft and smart modular structure (SMS) actuated by SMA wires *Bioinspir. Biomim.* **11** 056012

[42] Scherngell H and Kneissl A 2002 Generation, development and degradation of the intrinsic two-way shape memory effect in different alloy systems *Acta. Mater.* **50** 327–41

[43] Fauroux J C 2015 *Synthesis, design, modelling and experimentation of innovative machines - Application to agile mobile robots* Habilitation report, Université Blaise Pascal, France, 8th July 2015; 343 p

[44] Fauroux J C, Chapelle F and Bouzgarrou B C 2006 A new principle for climbing wheeled robots: serpentine climbing with the OpenWheel platform. In: *Intelligent Robots and*

Systems (Beijing, China, October 9-13, 2006) IEEE/RSJ International Conference on (New York, NY, USA: IEEE) pp. 3405–10

[45] Mammano G S and Dragoni E 2011 Modelling of wire-on-drum shape memory actuators for linear and rotary motion *J. Intell. Mater. Syst. Struct.* **22** 1129–40

[46] Mekaouche A, Chapelle F and Balandraud X 2015 FEM-based generation of stiffness maps *IEEE Trans. Robot.* **31** 217–22

[47] Mekaouche A, Chapelle F and Balandraud X 2016 Using shape memory alloys to obtain variable compliance maps of a flexible structure: concept and modeling *Meccanica* **51** 1287–99

Table 1. Parameters chosen for finite element simulations.

	Parameter	Value
SMA wire	Young modulus, E	60 GPa
	Poisson's ratio, ν	0.3
	Diameter	1 mm
ABS helix	Young modulus E_{ABS}	1.55 GPa
	Poisson's ratio, ν_{ABS}	0.35
	Yield stress *Re*	5 MPa
	Radius, *R*	44 mm
	Pitch, *i*+*b*	22 mm
	Number of turns, N_t	5

Table 2. Results of numerical simulations, guaranteeing the full reversibility of the rotation movement.

Parameter	Value
Strain of SMA wire in martensitic state, ε_{SMA}	0.62%
Width of helix cross section, b	12 mm
Height of helix cross section, h	4 mm
Obtained rotation angle for one turn, $\theta_{one\text{-}turn}$	30.3°

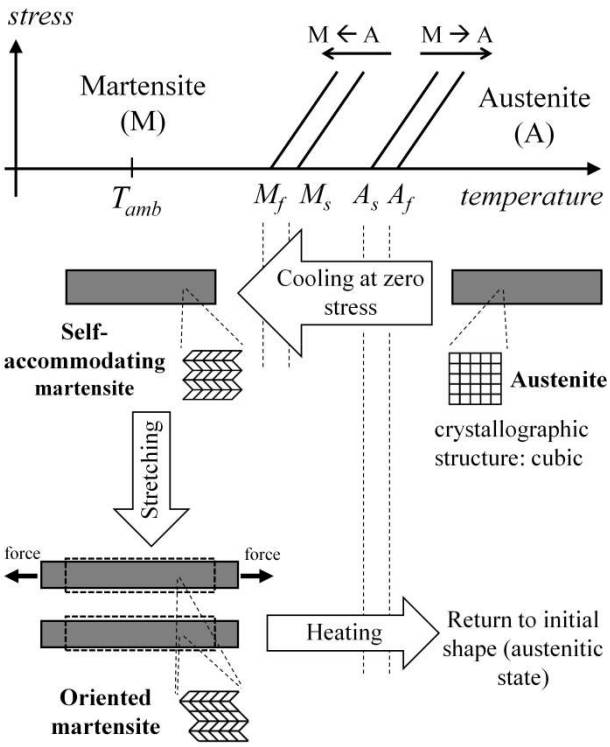

Figure 1. Simplified state diagram of a SMA and steps for the one-way memory effect.

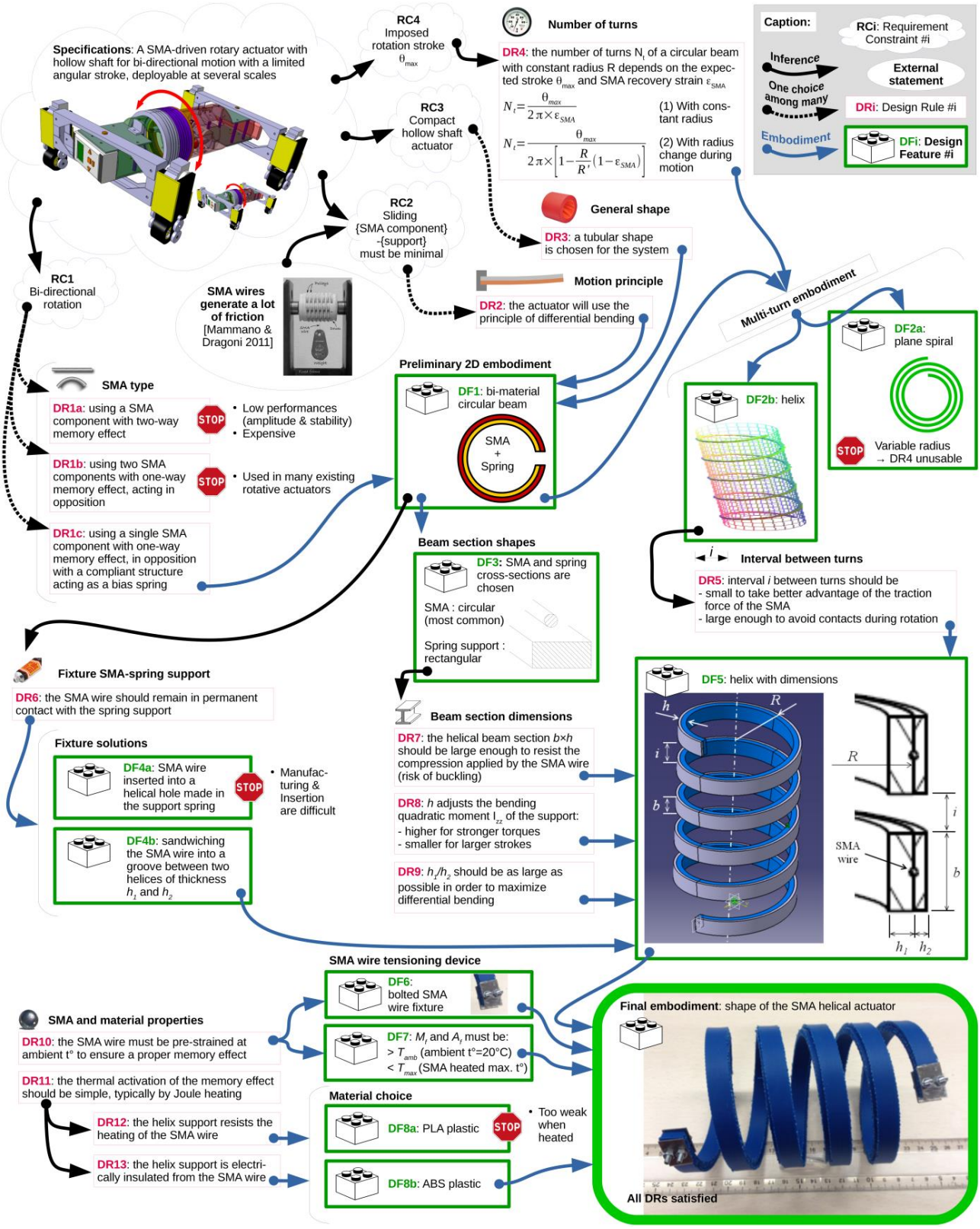

Figure 2. Design method based on the chaining of design rules.

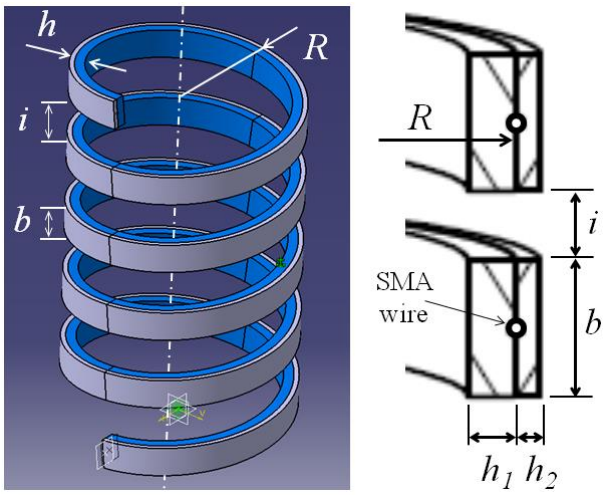

Figure 3. Geometric parameters for the helical structure.

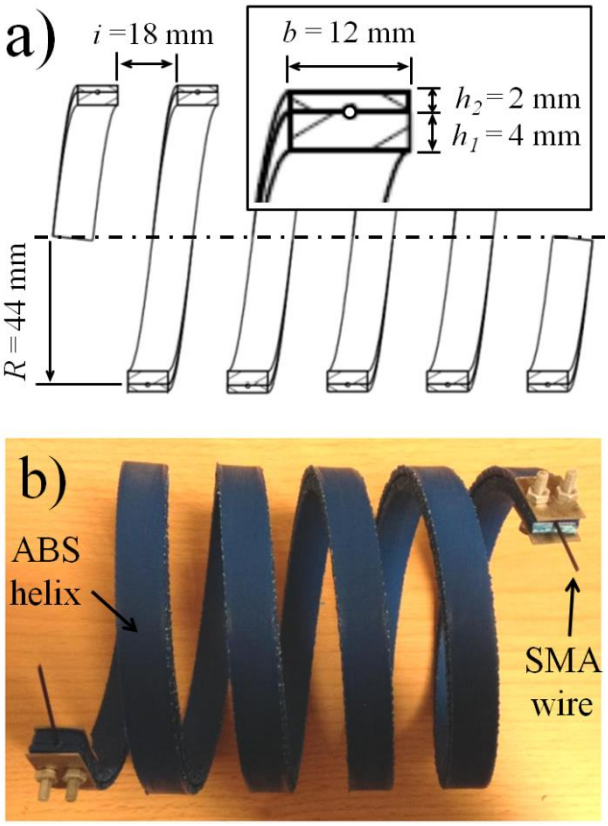

Figure 4. First prototype of SMA-driven rotary actuator: a) cross-section of the system, b) photo of the system. A 3D-printed ABS helix was used as a supporting structure, and a Ni-Ti-based SMA wire was placed in a groove between the two parts of the helix.

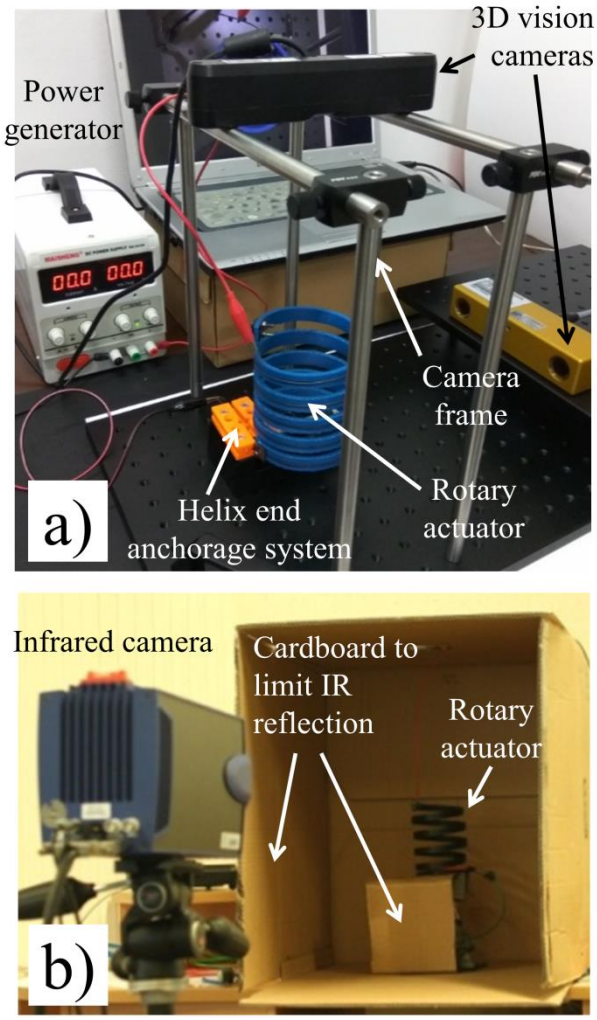

Figure 5. Experimental set-up: a) use of 3D vision cameras to measure the movement of the free end of the helix, b) use of an infrared camera to measure temperature variations during the thermal activation of the SMA wire.

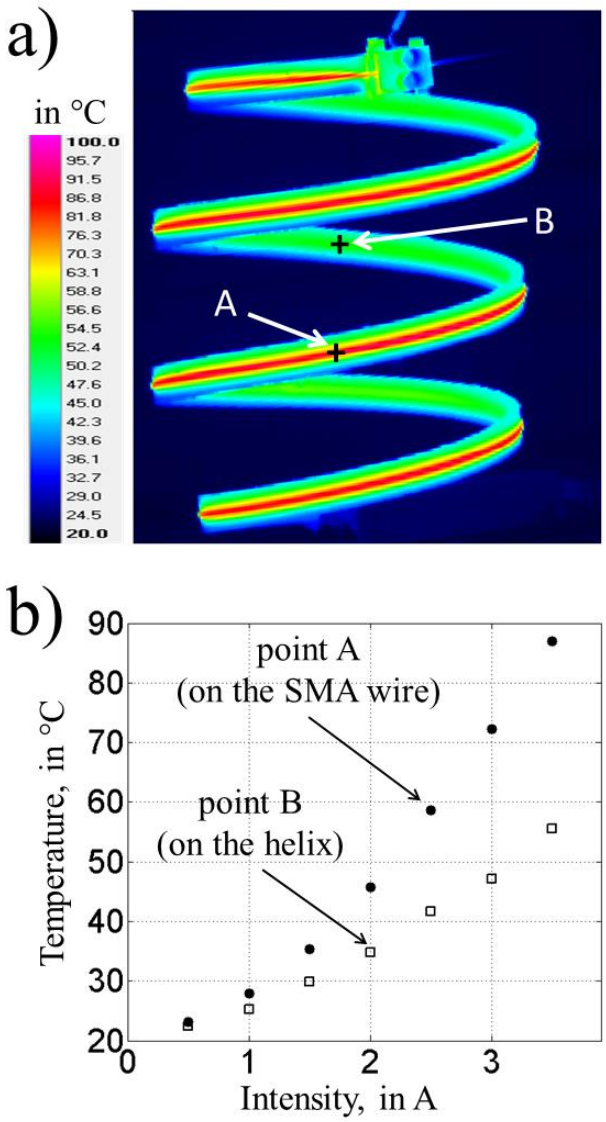

Figure 6. Thermal analysis of the first prototype: a) surface temperature in steady-state regime for an electric current intensity of 3.5 A, b) steady temperature at points A and B for different current intensities. Point A is located on the external radial surface. Point B is located on the internal radial surface of the helix.

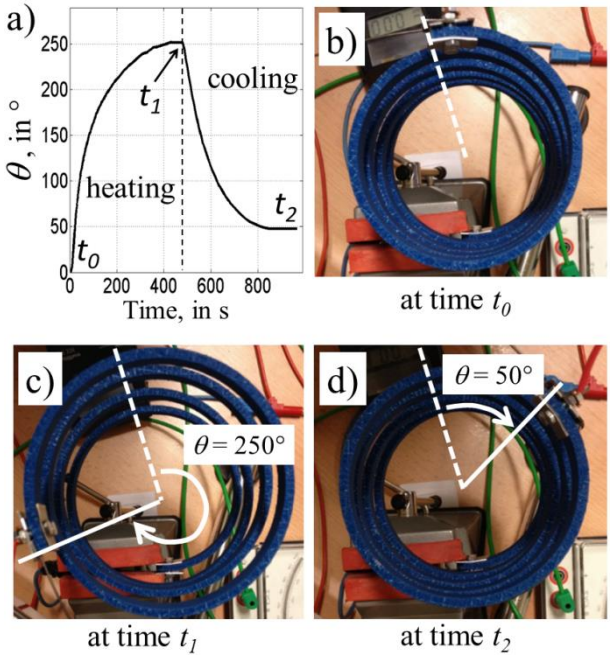

Figure 7. Variation in rotation angle θ during a thermal cycle on the first prototype. Bidirectional rotation was successfully obtained, but a residual angle remained at the end of the test (time t_2).

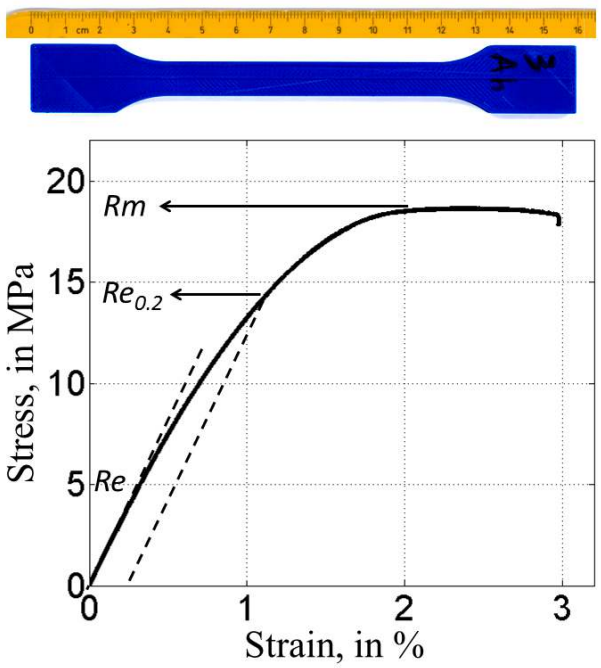

Figure 8. Strain-stress curve in tension of the 3D-printed ABS material.

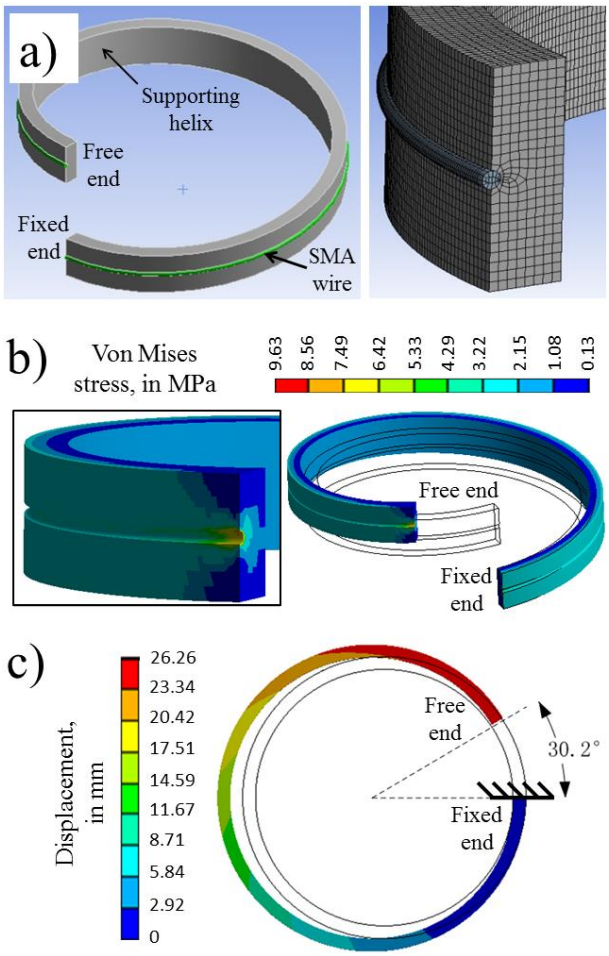

Figure 9. Finite element analysis performed: a) geometry and mesh of one turn of the helix with SMA wire, b) Von Mises stress field using the parameters in Tables 1 and 2, c) top view before and after the thermal activation of the SMA wire.

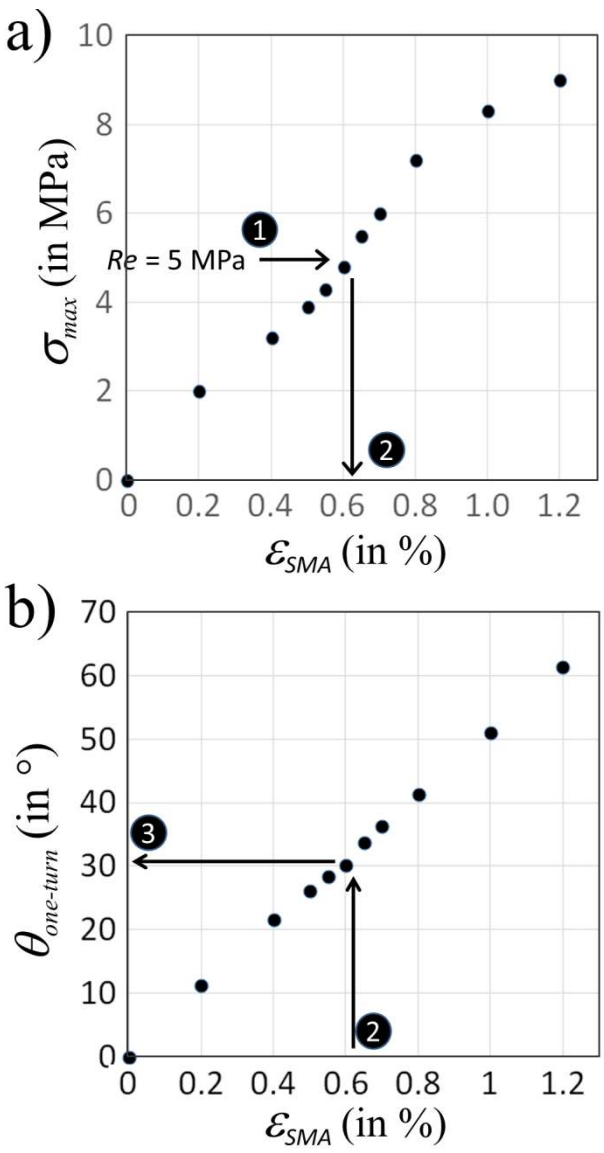

Figure 10. Identification of the recoverable strain ε_{SMA} of the SMA wire from simulations, with b = 12 mm, h = 4 mm and parameters given in Table 1: a) maximum Von Mises stress σ_{max} as a function of ε_{SMA}, b) rotation angle $\theta_{one\text{-}turn}$ as a function of ε_{SMA}.

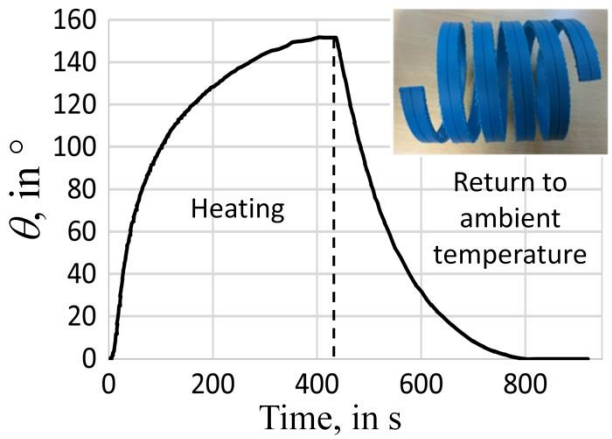

Figure 11. Variation in the rotation angle θ during a thermal cycle for the second prototype using an electric current intensity of 3.5 A.

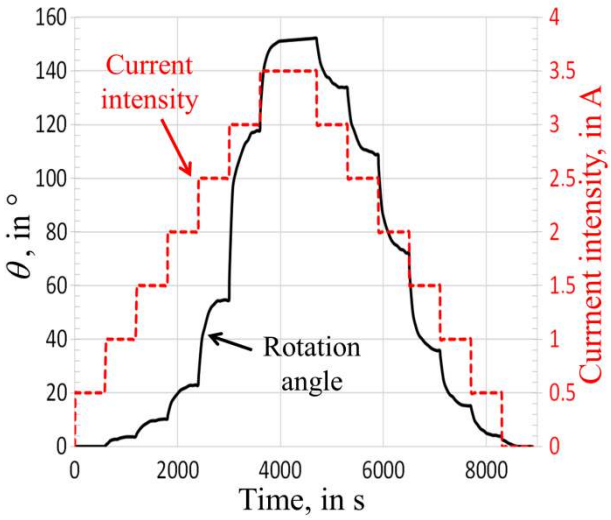

Figure 12. Variation in the rotation angle θ during a thermal cycle for the second prototype, with current intensities varying in steps of ±0.5 A.

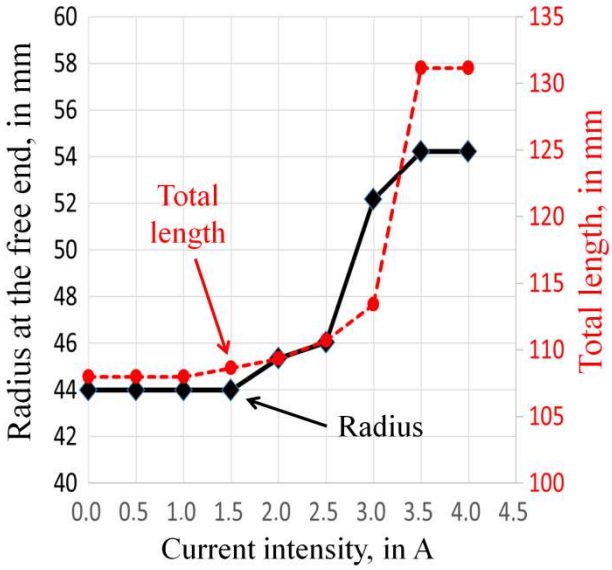

Figure 13. Variations in the total length (along the helix axis) and the radius at the free end of the helix (perpendicularly to the helix axis) as a function of current intensity.